LUND UNIVERSITY

MASTER'S THESIS

Development of a temperature control system for spectroscopic measurements with rare-earth doped crystals

QUANTUM INFORMATION GROUP, LUND UNIVERSITY, SWEDEN

Author:

Sijia HUANG

Supervisor:

Diana SERRANO

Professor:

Stefan KRÖLL

April 22, 2014

Popular science

Rare-earth ions have for a long time been seen as the “modern light source” because of their multiple energy levels. They have the potential to efficiently emit light with different colors. After studying the rare-earth ions further, people found the emitted photons have a long coherence time. It means that the rare-earth ions, which have been discussed to be used as information carriers and processors in quantum computers, can stay at their excited states for a long time. The new carriers for the information are called qubits (short for quantum bit). In contrast with the original carrier, or bit, in the case of the qubits, a superposition state between the states 1 and 0 can be created. The experimental work on rare-earth ions for quantum computing is carried out at low temperatures, around 4 Kelvin (-269 °C). This work has involved the development of a temperature measurement system for keeping track of the sample temperatures both during the cooling down period and during the experiments. The temperature monitoring system has then been tested in conjunction with spectroscopic measurements of the rare earth ion energy levels. It is important to have an initial version of the rare-earth ions energy levels. Hence, by measuring the emission fluorescence spectra, people can know more about the properties of the rare-earth ions. In the present case, the spectra have been measured as a function of temperature going from room temperature to -269 °C.

Eu^{3+} ions are one of the most interesting candidates for quantum information. Figure 1 shows the optical setup used to measure the fluorescence spectra.

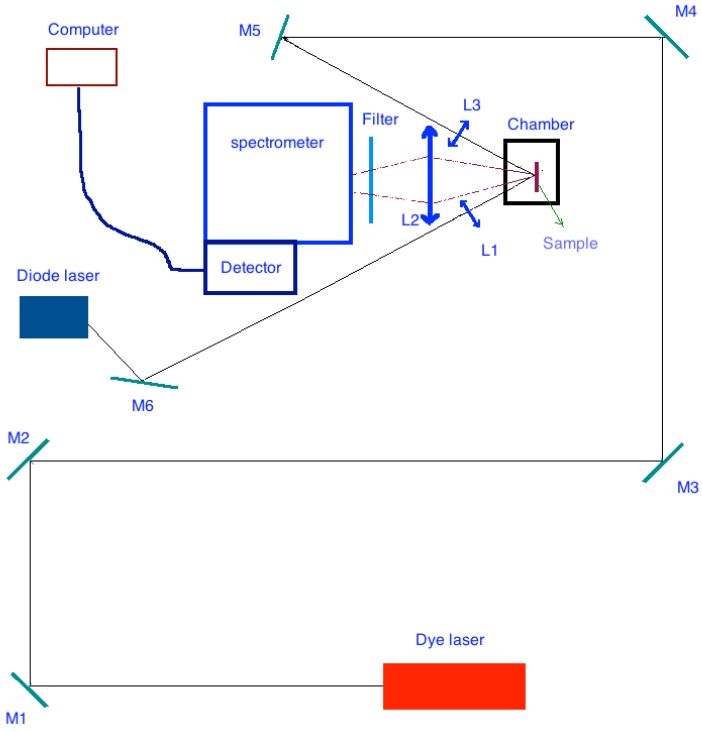

Figure 1. Fluorescence measurement setup.

Two different laser systems were used to excite the Eu^{3+}: Y_2SiO_5 and Ce^{3+}-Eu^{3+}: Y_2SiO_5 samples. Mirrors M1 to M6 are used for directing the excitation beams from the two lasers to the sample chamber. The laser beams from the diode and dye lasers are focused onto the sample using lenses L1 and L3 respectively. The emission light is collected by lens L2 and then sent into the spectrometer. The fluorescence spectra are finally recorded by the detector. A computer afterwards is used to analyze the recorded fluorescence data.

Abstract

This thesis describes the development of a temperature control system for optical spectroscopy experiments with rare-earth doped samples. Low temperature emission spectra were afterwards recorded for a series for Eu^{3+} singly doped and Ce^{3+}, Eu^{3+} codoped Y_2SiO_5 samples. The analysis and assignment of the different energy transitions is presented.

The experimental setups used in this thesis involve the optics part, the electronic part and the cooling down system. For the optical measurements, two kinds of pumping laser were used: Dye laser (580 nm) and UV laser (370 nm). A suitable optics system was designed for the collection of fluorescence signals. Electronic circuits were on the other hand built to connect two thermal sensors within the cryostat used for the optical measurements. Two reference temperature sensors were set up so that they could be readout simultaneously by using a switch connected with a temperature monitor. A good control of the cooling down process and the final temperature reached by the samples under investigation is fundamental for spectroscopic investigations performed at cryogenic temperatures as the ones described here.

Contents

1. Introduction

1.1 Background

The rapid development of the optical technologies during the past years has notably increased the demand on luminescent materials for a large variety of applications. In this context, the rare-earth solids are particularly interesting candidates as they present multiple energy levels and they have the potential to efficiently emit light at different wavelengths. The rare-earth ions or "lanthanides", act as optically active centers when they are introduced into a host material as dopants. The particularity of these ions resides in the fact that the optically active layer, which is the 4f electronic shell, is protected from the crystal environment by fulfilled outer electronic shells. This screening effect leads in particular to narrow optical transitions and long fluorescence lifetimes for the rare-earth ions in crystals compared to other luminescent solids [1].

Nowadays, the rare-earth doped materials can be found in a large number of optical applications, both in industry and science. For instance, in the field of laser technologies, rare-earth doped materials can be used as gain media. Typically, the Nd^{3+}: YAG laser, is a rare-earth based solid-state laser. However, not only Nd^{3+}, but also ions such as Yb^{3+}, Er^{3+} and Tm^{3+} can be doped into YAG or other crystalline hosts to be used as laser gain media [2]. On the other hand, fiber lasers in which the active gain medium is an optical fiber doped with rare-earth elements such as Er^{3+}, Yb^{3+}, Nd^{3+}, Dy^{3+}, Pr^{3+}, and Tm^{3+}, constitute another important rare-earth based solid-state laser technology. Glass fibers doped with rare earths are also broadly used as optical amplifiers for telecommunications. The EDFA (ytterbium doped fiber amplifier) is one of them [3].

Besides the above described applications, the long optical lifetimes and coherence times make of the rare-earth solids interesting candidates for quantum information. In the quantum information field, a new information carrier or qubit is defined. The qubit is in particular encoded in the hyperfine levels of the rare-earth dopants. In contrast with the original information carrier, or bit, in the case of the qubits, a superposition state between the states 1 and 0 can be created [4]. Materials such as Eu^{3+}: Y_2SiO_5, investigated in this thesis, and Pr^{3+}: Y_2SiO_5 are found among the most interesting for quantum storage and quantum information processing.

1.2 Purpose of this thesis

1.2.1 Development of a temperature control system for optical spectroscopy experiments with rare-earth doped samples

The optical emission and absorption features of rare-earth ions in crystals are temperature dependent. In particular, exploiting the coherence properties of the rare earths requires cooling the crystals down to cryogenic temperatures (below 4K). In order to monitor the cooling down process, and with the aim of knowing the final temperatures reached by the samples, a temperature control system, implemented into a cold finger cryostat has been developed during this thesis. The system is based on two temperature sensors connected directly to the sample and to the sample holder respectively. The detail of the setup will be shown in section 3.

1.2.2 Experimental study of the Eu^{3+} emission spectrum at different temperatures

The Eu^{3+}-Ce^{3+} pair has been proposed for quantum computing applications, where Eu^{3+} plays the role of qubit ion and Ce^{3+} that of readout ion. As the information carrier, Eu^{3+} is asked to have a long coherent time while in the case of Ce^{3+}, a short excited state lifetime is aimed for the detection of fluorescence after interaction with the qubit ion. A first spectroscopic investigation of this codoping is carried out in this thesis. Eu^{3+} fluorescence spectra were recorded at different temperatures for several Eu^{3+} singly doped Y_2SiO_5 samples and Eu^{3+}-Ce^{3+} codoped Y_2SiO_5 samples, both under direct Eu^{3+} excitation and also under Ce^{3+} excitation after subsequent energy transfer $Ce^{3+} \rightarrow Eu^{3+}$.

1.3 Outline of this thesis

In section 2, the theory of the energy level split of rare-earth ions, the properties of the rare-earth doped materials and the optical emission and absorption processes have been introduced. In section 3, we show how the experimental setups used in the thesis were designed and how the experiments were done. In section 4, the temperature control system is tested under different conditions and the energy transitions of Eu^{3+} ions were analyzed. In section 5, some ideas about potential improvement of the experimental setups are suggested and the conclusion of the work is discussed.

2. Theory

2.1 Energy levels of Rare-earth ions in crystals

In the element periodic table, there is an extra bar out of the main table. The elements with atomic number between 57 (Lanthanum) and 71 (Lutetium) are named Lanthanides or rare earth elements. Because of their unfilled and optically active 4f shell, the lanthanides are usually referred to as 4f element. They commonly exist in the nature as doubly or triply charged ions. When trivalent rare earth ions doped in host materials they exhibit stability, small reabsorption losses and high luminescent quantum yields [5].

In the free space, the energy states of an atom with n electrons are given by the time-independent Schrödinger equation:

$$\mathcal{H}\boldsymbol{\psi}(\boldsymbol{r}_1, \dots, \boldsymbol{r}_n) = E\boldsymbol{\psi}(\boldsymbol{r}_1, \dots, \boldsymbol{r}_n) \tag{2.1}$$

in which $\boldsymbol{\psi}(\boldsymbol{r}_1, \dots, \boldsymbol{r}_n)$ is the wavefunction of eigenvalue E, and $\mathcal{H}$, is the Hamiltonian for the n-electron system which takes the form:

$$\mathcal{H} = \sum_{\mathrm{i}=1}^{\mathrm{n}} \left(-\frac{\hbar^2}{2\mathrm{m}} \frac{\partial^2}{\partial \boldsymbol{r}^2} - \frac{\mathrm{Ze}^2}{4\mathrm{e}\epsilon_0 \boldsymbol{r}_i} \right) + \sum_{\mathrm{i}=1}^{\mathrm{n}} \xi(\boldsymbol{r}_i)\boldsymbol{\ell}_{\mathrm{i}}.\mathbf{s}_{\mathrm{i}} + \frac{1}{2} \sum_{i \neq j} \sum_{\mathrm{i}=1}^{\mathrm{n}} \frac{\mathrm{e}^2}{4\pi\epsilon_0 |\boldsymbol{r}_i - \boldsymbol{r}_j|} \tag{2.2}$$

The many-electron Hamiltonian is consisted by three parts, the first part being kinetic and potential energy operators for each electron of a nucleus of charge Ze; the second part describing the spin-orbit coupling interaction and the third part representing the inter-electron Coulomb repulsion. $|r_i - r_j| = r_{ij}$ is the electrostatic repulsion between the two electrons at $\mathrm{r_i}$ and $\mathrm{r_j}$ [6]. Approximated wavefunctions can be found for the n-electron system under the *central field approximation.* This approximation assumes that a large part of the repulsion between the electrons can be referred to as $\mathrm{S}(\mathbf{r_i})$ [6]. Thus,

$$\mathcal{H} = \mathcal{H}_{\mathrm{cf}} + \mathcal{H}' + \mathcal{H}_{\mathrm{so}} \tag{2.2'}$$

in which

$$\mathcal{H}_{\mathrm{cf}} = \sum_{i=1}^{n} \left(-\frac{\hbar^2}{2\mathrm{m}} \frac{\partial^2}{\partial \boldsymbol{r}^2} - \frac{\mathrm{Ze}^2}{4\mathrm{e}\epsilon_0 \boldsymbol{r}_i} + \mathrm{S}(\mathbf{r_i}) \right) \tag{2.3}$$

$$\mathcal{H}_{\mathrm{so}} = \sum_{\mathrm{i}=1}^{\mathrm{n}} \xi(\boldsymbol{r}_i)\boldsymbol{\ell}_{\mathrm{i}}.\mathbf{s}_{\mathrm{i}} \tag{2.4}$$

$$\mathcal{H}' = \frac{1}{2}\sum_{i\neq j}\sum_{\mathrm{i=1}}^{\mathrm{n}} \frac{\mathrm{e}^2}{4\pi\epsilon_0|\boldsymbol{r}_i - \boldsymbol{r}_j|} - \sum_{\mathrm{i=1}}^{\mathrm{n}} \mathrm{S}(\mathbf{r_i}) \tag{2.5}$$

For light atoms the effect of $E' \gg \mathrm{E_{so}}$, so that wavefunctions, namely *LS terms* of energy $E(\,^{2S+1}L)$, are found for $\mathcal{H}_0 + \mathcal{H}'$. The spin-orbit interaction is next taken into account (*LS coupling* or *Russel-Saunders coupling*), provoking the degenerated ^{2S+1}L terms to split into several $^{2S+1}L_J$ terms with $J = |L + S|$ and degeneracy equal to $2J + 1$ [6]. On the other hand, heavier atoms endure the effect of the spin-orbit interaction, $E_{so} \gg E'$. In that case, we consider the coupling of the spin and orbital angular momentum on individual electrons (j states with $j_1 = l_1 + s_1, j_2 = l_2 + s_2$ for individual electrons) and then, the coupling of the j states through $\mathcal{H}'$ (*j-j coupling*) [7].

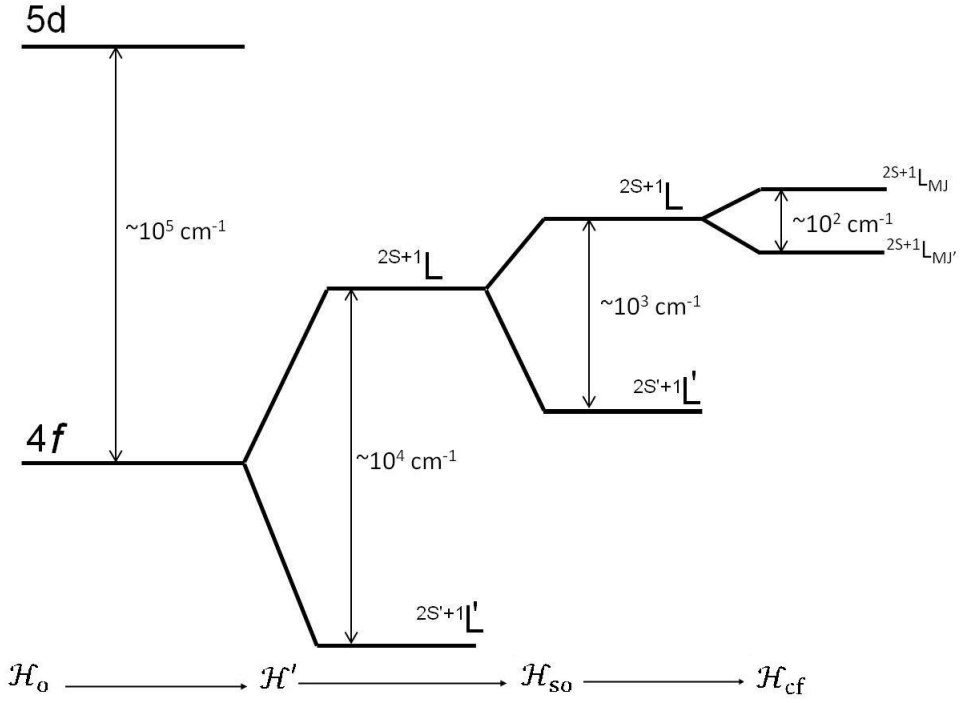

Figure 2.1. 4*f* energy levels splitting under the effect of different interactions

Eventually, when comparing the $\mathcal{H}'$ and $\mathcal{H}_{\mathrm{so}}$ with the same quantum number J but different quantum numbers L and S takes place (*intermediate coupling*), the wavefunctions are difficult to determine. The rare-earth ions are in this group. Thus the $4f^n$ energy levels are expressed as $^{2S+1}L_J$ Russel-Saunders terms (*L-S coupling approximation*). Their final position is then derived from experimental data of the free-ion emission spectra. The *Dieke diagram* was reported by Dieke and Crosswhite in 1963, describing the $4f^n$ energy levels [8].

$$\mathcal{H} = \mathcal{H}_0 + \mathcal{H}' + \mathcal{H}_{\mathrm{so}} + \mathcal{H}_{\mathrm{cf}} \tag{2.6}$$

For instance, in a crystal environment, the $^{2S+1}L_J$ leves split into a number of

sub-levels (*Stark sub-levels*) due to the interaction between the $4f^n$ electrons and the electric field created by the crystal lattice. Because the 4*f* electrons are partially screened by the filled $5s^2 5p^6$ outer shells, the optically-active 4*f* electrons are almost not affected by the crystal field. Thus, the spin-orbit coupling caused splitting is much stronger than the splitting caused by the interaction with the crystal field ($\mathcal{H}_{\mathrm{cf}}$), which is thus treated as a perturbation on the free-ion energy levels:

Table 2.1. Expected splitting for a $^{2S+1}L_J$ level according to the site symmetry.

Splitting	*J=0*	*J=1*	*J=2*	*J=3*	*J=4*	*J=5*	*J=6*	*J=7*	*J=8*
2J+1	1	3	5	7	9	11	13	15	17
Cubic	1	1	2	3	4	4	6	6	7
Hexagonal	1	2	3	5	6	7	9	10	11
Trigonal	1	2	3	5	6	7	9	10	11
Tetragonal	1	2	4	5	7	8	10	11	13
Orthorhombic	1	3	5	7	9	11	13	15	17
Monoclinic	1	3	5	7	9	11	13	15	17
Triclinic	1	3	5	7	9	11	13	15	17

Analyzing the crystal field is a complicated problem. However, we can think it in a simple way by using the point charge model. The electrostatic crystal field being caused by lattice ions is represented by point charges supposed fixed in their lattice position. The crystal-field Hamiltonian takes then the form:

$$\mathcal{H}_{\mathrm{cf}} = \frac{1}{4\mathrm{f}\epsilon_0} \sum_{\mathrm{i}} \sum_{\mathrm{l}} \frac{\mathrm{Z_l e}^2}{|\boldsymbol{R}_l - \boldsymbol{r}_i|} \tag{2.7}$$

where the summations is done over all 4*f* electrons and ligands. The development of $|\boldsymbol{R}_l - \boldsymbol{r}_i|^{-1}$ in a base of spherical harmonics leads to:

$$\mathcal{H}_{\mathrm{cf}} = \sum_{\mathrm{k,q}} \sum_{\mathrm{l}} \mathbf{B}_{\mathrm{q}}^{\mathrm{k}} \mathbf{C}_{\mathrm{q}}^{\mathrm{k}}(\theta, \Phi) \tag{2.8}$$

Which presents the crystal field usually doped by rare-earth ions. $\mathbf{B}_{\mathrm{q}}^{\mathrm{k}}$ is the crystal field parameters. The crystal field experienced by the optically-active 4*f* electrons notably reflects the symmetry of the crystalline environment, especially the symmetry regarding the nearest ligands (local symmetry). The splitting of the $^{2S+1}L_J$ energy levels is for instance more important when the local site symmetry is low as showed [9].

2.2 Rare-earth ions and doped crystals

2.2.1 Energy level of Eu^{3+} and Ce^{3+} ion

The energy transitions of the Eu^{3+} ions investigated here are 4f-4f transitions. The Eu^{3+} energy level scheme is shown in Figure 2.2. Europium represents a particular case within the lanthanide series as some of its transitions, in particular that from the ground state $^7F_0$ to the $^5D_0$ singlet are highly forbidden for violating electric dipole selection rules ($\Delta J=0$). As we will see further in this thesis, the $^5D_0 \rightarrow {}^7F_0$ emission line can nevertheless be observed [10].

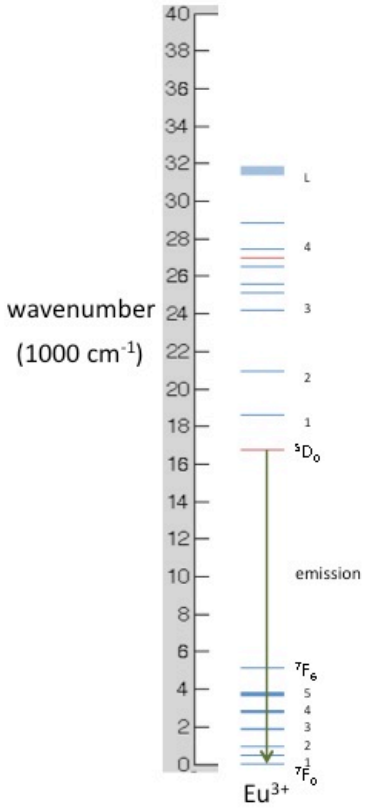

Figure 2.2. Eu^{3+} energy level scheme

In the case of Ce^{3+}, the 4f-5d transition is investigated. The 5d electronic shell, contrarily to the 4f layer, is highly perturbed by the crystalline environment, which gives rise to broad absorption and emission bands. For instance, the Eu^{3+} transitions considered here present a broadening of few GHz while the Ce^{3+} emission band covers several hundreds of THz.

2.2.2 The host material: Y_2SiO_5

The Y_2SiO_5 crystal presents a monoclinic cell with C_{2h}^6 symmetry. That contains a two-fold rotation axis and one mirror plane perpendicular to the rotation axis. Eight Y_2SiO_5 molecules are included in a unit cell [11]. Y_2SiO_5 present important advantages to be used as host material for quantum information applications, as it has low nuclear magnetic moments. Another reason is that, it has low abundance of isotopes with non-zero nuclear magnetic moments [11]. As a result, it enables long coherence times, limiting the homogeneous broadening. The dopant ions (Eu^{3+} in this case) are replaced by the Y^{3+} ions randomly. Since the dopant ions present a slightly different ionic radius than the yttrium ions, they distort the lattice around them. In consequence, the local environment of the different dopants is slightly different, which results in different absorption and radiation energies for each single ion in the host.

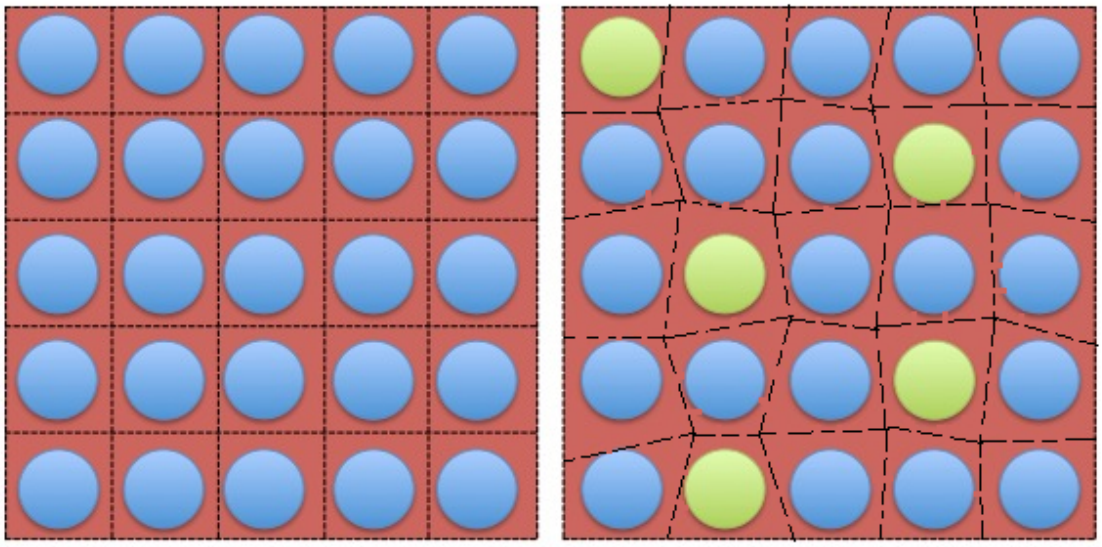

Figure 2.3. Illustration of the Eu^{3+}: Y_2SiO_5 crystal structure. The blue spots are the Y^{3+} ions, and the green spots are the doped Eu^{3+} ions.

This gives rise to the so-called inhomogeneous broadening. The inhomogeneous broadening phenomenon is typical from solids.

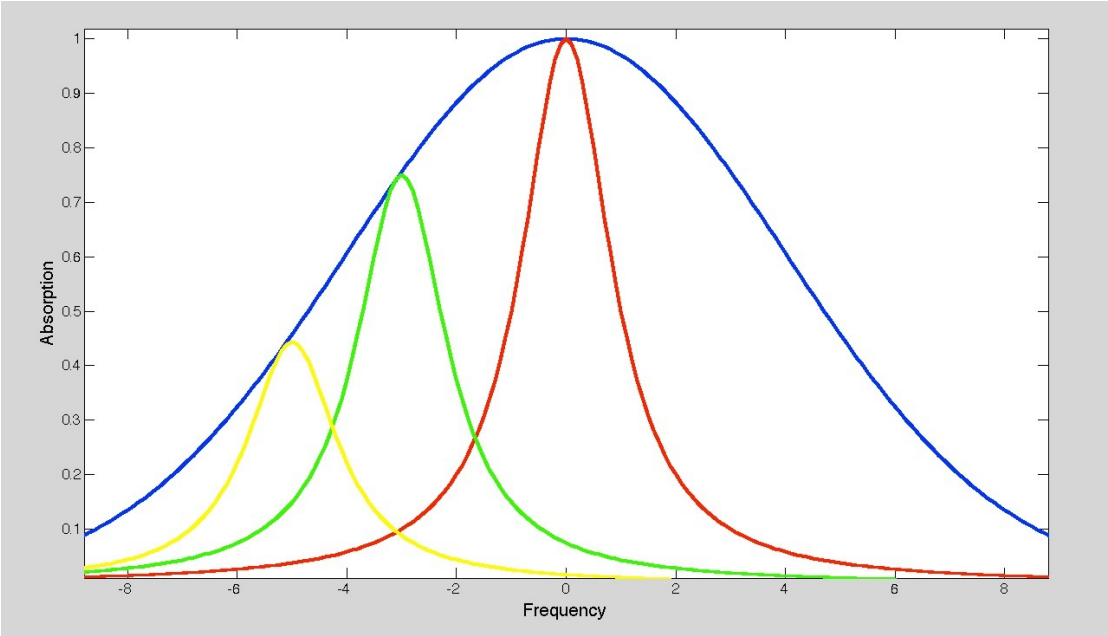

Figure 2.4. Homogeneous absorption lines included within the inhomogeneous broadening. The blue line represents inhomogeneously broadened optical transition. The yellow, green and red lines represent the natural broadening (homogeneous) for different subgroups of atoms.

2.3 Light-mater interaction

2.3.1 Optical absorption and emission processes

The mechanism of fluorescence is illustrated in Figure 2.4, according to an ideal two energy level model. After absorbing the energy, the electron is promoted to the excited state. Then this excited electron can spontaneously decay to the ground level and emit a photon with the energy corresponding to the difference of the two energy levels. In a real case, the presence of multiple energy levels makes the emission transitions possible from the excited level to any of the lower levels. Thus, the emission wavelength is not single, but a continuous band or discrete lines [11].

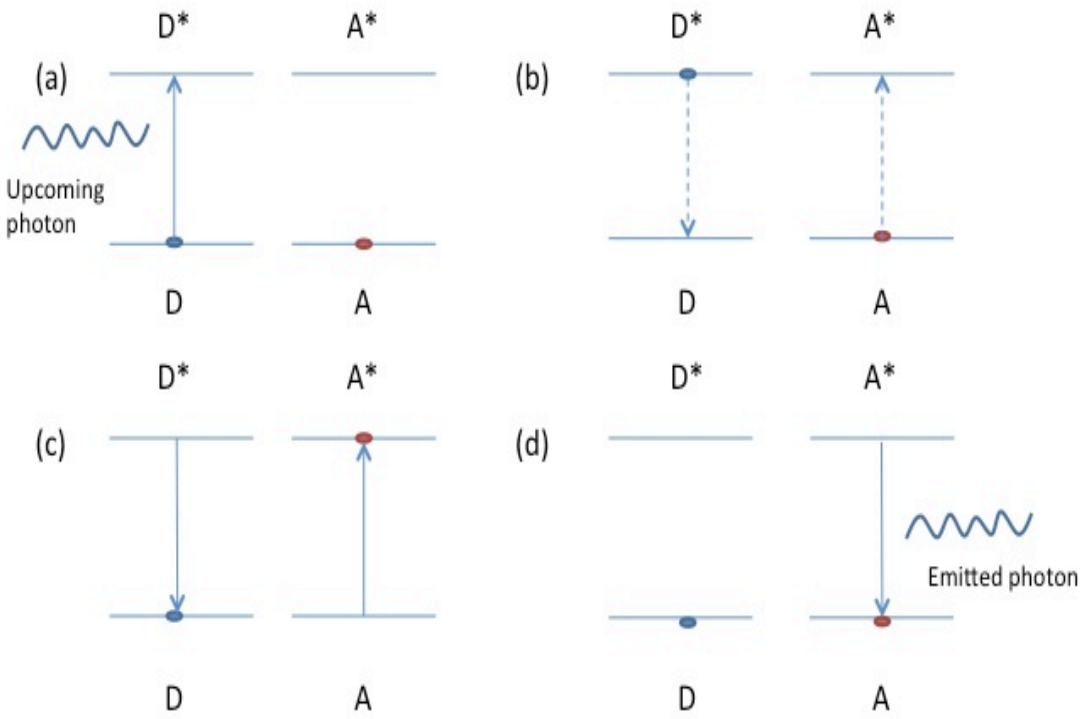

Figure 2.5. (a) Absorption of energy by the donor, (b) energy transfer, (c) acceptor ion excited and (d) emission from the acceptor ion.

2.3.2 Förster resonance energy transfer (FRET)

The energy transfer processes were described by Dexter (1953) as being able to take place between impurity centers in condensed media [12]. The energy transfer mechanism takes place as follows. An upcoming photon is absorbed by a first dopant ion or "donor", being promoted to its excited state. The energy is then transferred to a second ion or "acceptor". Finally, a photon is emitted by the acceptor ion when this one relaxes back to its ground state. The classical approach considers the non-radiative energy transfers to occur by direct electric multipole interaction between donors and acceptors [13]. The energy transfer rate is generally given by:

$$W_{DA} = \frac{C_{DA}^{(n)}}{R^n}$$

In which $C_{DA}^{(n)}$ in the so-called transfer microparameter, depending on the overlap between the donor emission and the acceptor absorption, and R the donor-acceptor distance. In this thesis, we observe energy transfer from Ce^{3+} to Eu^{3+}

3. Methods

3.1 Description of the temperature monitoring system

3.1.1 Improving the thermal conductivity of the sample holder

The experiments in this thesis were carried out at low temperature. During these experiments, the samples are set into a copper crystal holder, which is directly in contact with a so-called cold finger (shown in Figure 3.1). The cold finger typically reaches temperatures below 4K as it is filled with liquid Helium. In this configuration, an efficient cooling down of the sample involves good thermal contacts and high thermal conductivity for the crystal holder. Materials such as gold, silver, and typically copper, have good thermal conductivities. Highly pure gold and silver are very expensive. In contrast, highly pure copper not only has very-low thermal resistivity, but also costs relatively less.

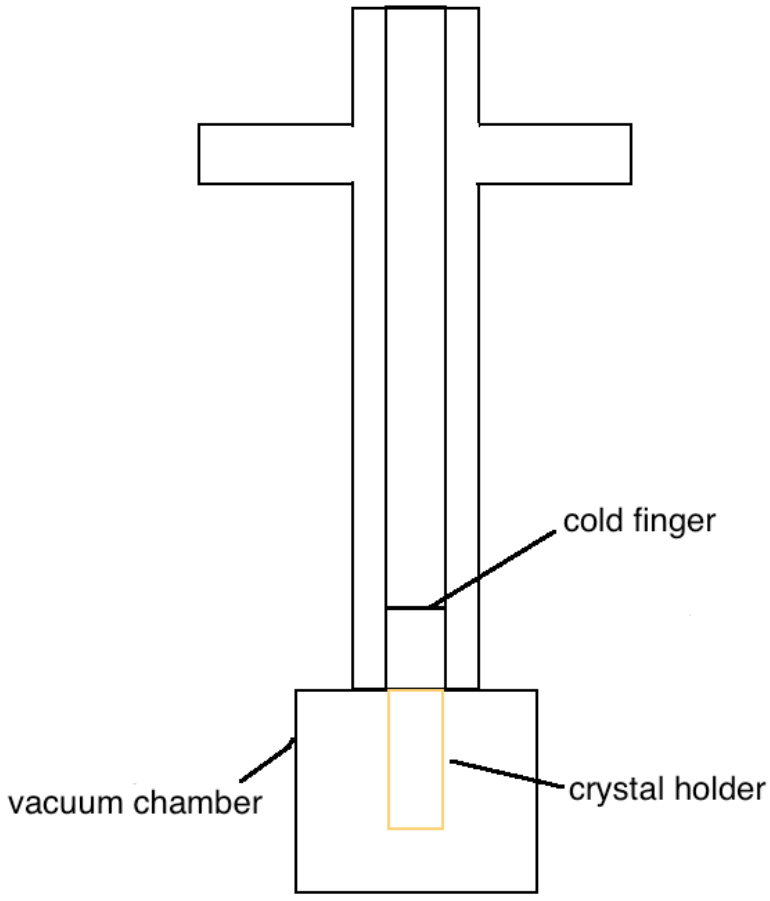

Figure 3.1. How the cold finger contact with the crystal holder

Thus, a high thermal conductivity is needed for the copper holder in order to transfer heat between the cold finger and the crystal sample efficiently. The crystal holder

used for the experiments was built from a piece of ultra-pure copper. A further reduction of the thermal resistivity can be achieved by annealing techniques. Copper, as any crystalline structure presents a certain stress related to the existence of defects such as grain boundaries and dislocations [14] . This is particularly true if the sample has been cast, bended or worked in any way. Actually, each time a metallic sample is worked it accumulates strain and gets harder. Annealing treatments have been shown helpful to homogenize and reduce stress in metals while improving their transport properties, both thermal and electrical. This treatment is well-known and often applied to metallic components of industrial equipment.

Procedure:

The copper was heated up to a temperature of 550 ^{o}C approximately within a protective Nitrogen atmosphere. Then, it was kept at this temperature for 3h30. Afterwards it was cooled back to room temperature with a cooling ramp of 2 degrees per minute. The protective atmosphere is required as copper readily oxidizes in contact with air, which drastically quenches the thermal conductivity. Examples of protective atmospheres are typically H_2, N_2 and Ar. Hydrogen seems nevertheless to be a bad election for copper due to its inability to prevent copper from oxidation. Nitrogen was here chosen as improvement of the thermal conductivity of a factor 3 has been reported after N_2 annealing [15].

After the annealing procedure the copper piece was treated with glacial acetic acid to remove surface copper oxides formed during the annealing process despite the protective atmosphere. Finally the holder was built and gold coated with the aim of obtaining a better surface quality to improve the thermal contact

3.1.2 Connection of the temperature sensors

In order to allow the active use of two temperature sensors within the cryostat, suitable circuits were designed. These two temperature sensors are Silicon diodes presented in CU and SD packages respectively, (shown in Figure 3.2). The CU sensor is used to measure the temperature of the crystal holder, while the SD sensor is attached directly to the sample to measure its temperature. A 4-lead wire connection is used to carry the electric signals. The wires needed for each of sensor were soldered onto a 4-pin connector (shown in Figure 3.2), so that the sensors can be plug and unplug easily according to the needs of the experiment.

Figure 3.2. Temperature sensor in CU package (left) and temperature sensor in SD package (right). The 4-pin connector used as plug is also shown in the photo.

Both of the sensors work in the same way by measuring the voltage drop of the sensor. The scheme describing how the measurement is done is shown in the following Figure 3.3 [16].

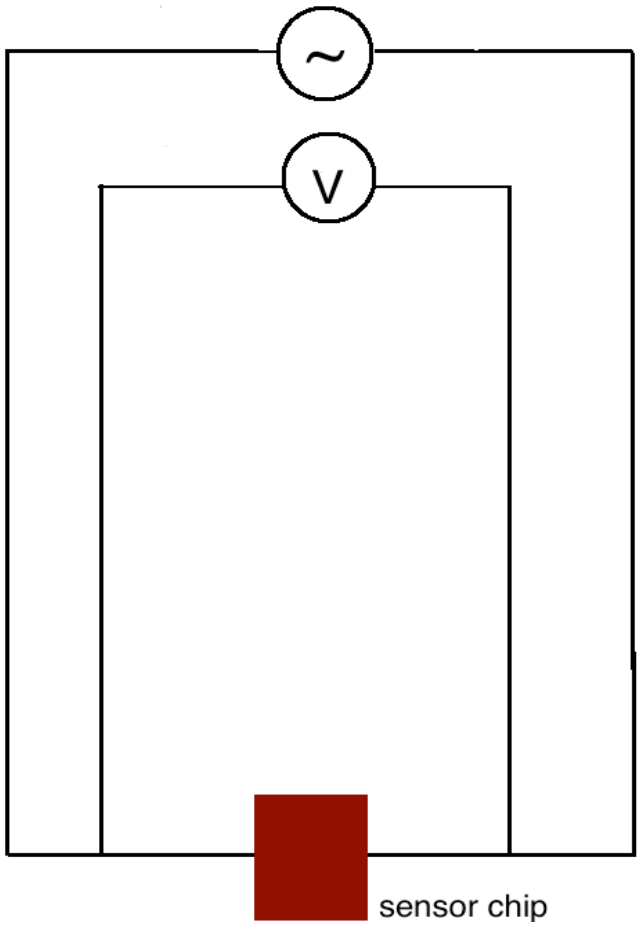

Figure 3.3. Thermal sensors 4-lead connection scheme.

The sensors were attached to the sample and sample holder as follows: the SD sensor was instead fixed between the sample and the plastic plate, which is shown in Figure 3.4 (a). It is actually pressed against the sample surface by the plastic plate. The plastic plate presents an optical opening (see figure) which allows the excitation laser beam to reach the sample during optical experiments. Figure 3.4 (b) displays the CU sensor. As shown, it is fixed in the same way as the SD sensor.

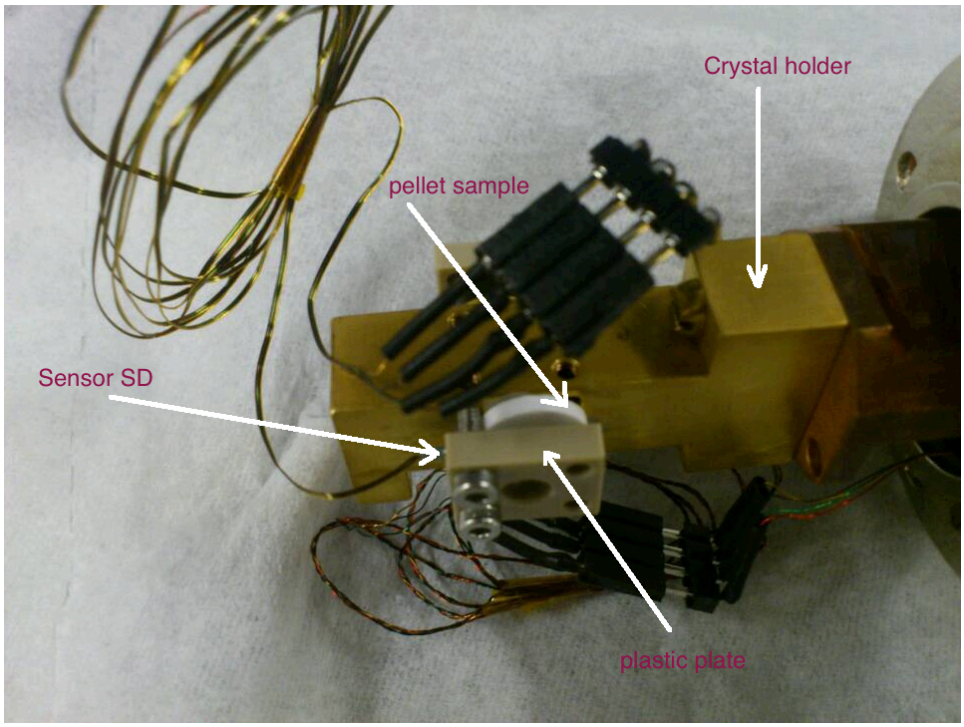

Figure 3.4 (a). SD sensor fixed over the sample surface.

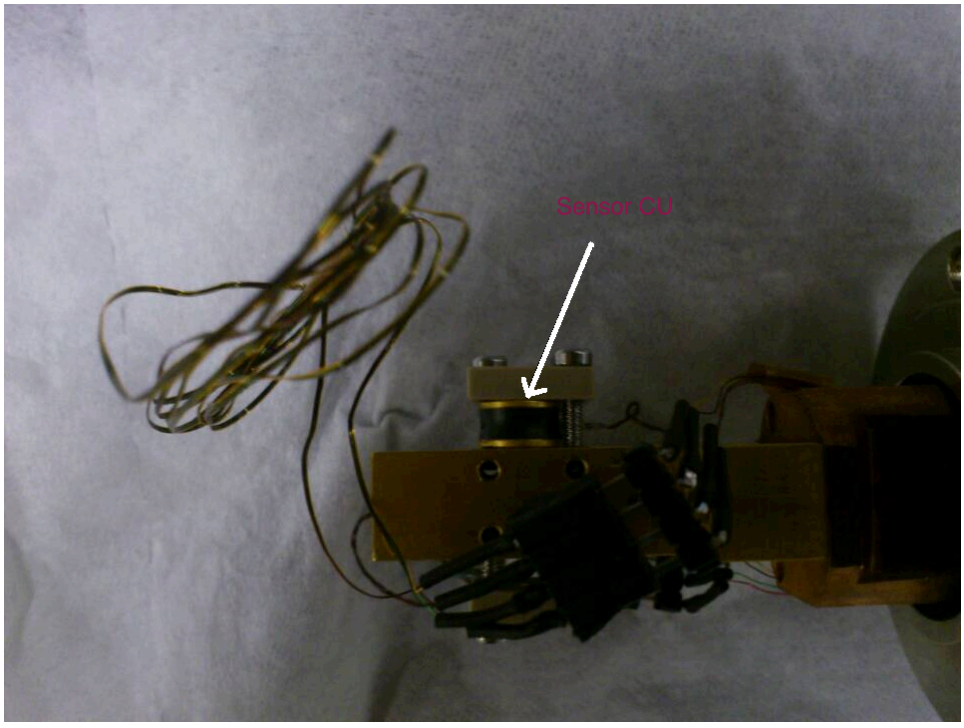

Figure 3.4 (b). CU sensor fixed over the crystal holder.

The wires leading the signals were rolled around the cryostat tube and soldered to one of the cryostat output ports (Figure 3.5).

Figure 3.5. Inner view of the cryostat.

In order to readout both sensors alternatively, a switch box (shown if Figure 3.6) is used. The blue cable is used to connect the switch to the temperature monitor. The two white cables are linked to the output port of the cryostat. Then, the temperature on the crystal holder and the crystal sample can be known. All cables used here are shielded to minimize capacitive coupled noise from other electrical sources. The metal shield can protect the internal electrical field (only caused by the signal) from external electric fields [17].

Figure 3.6 (a). The wire connection on the switch.

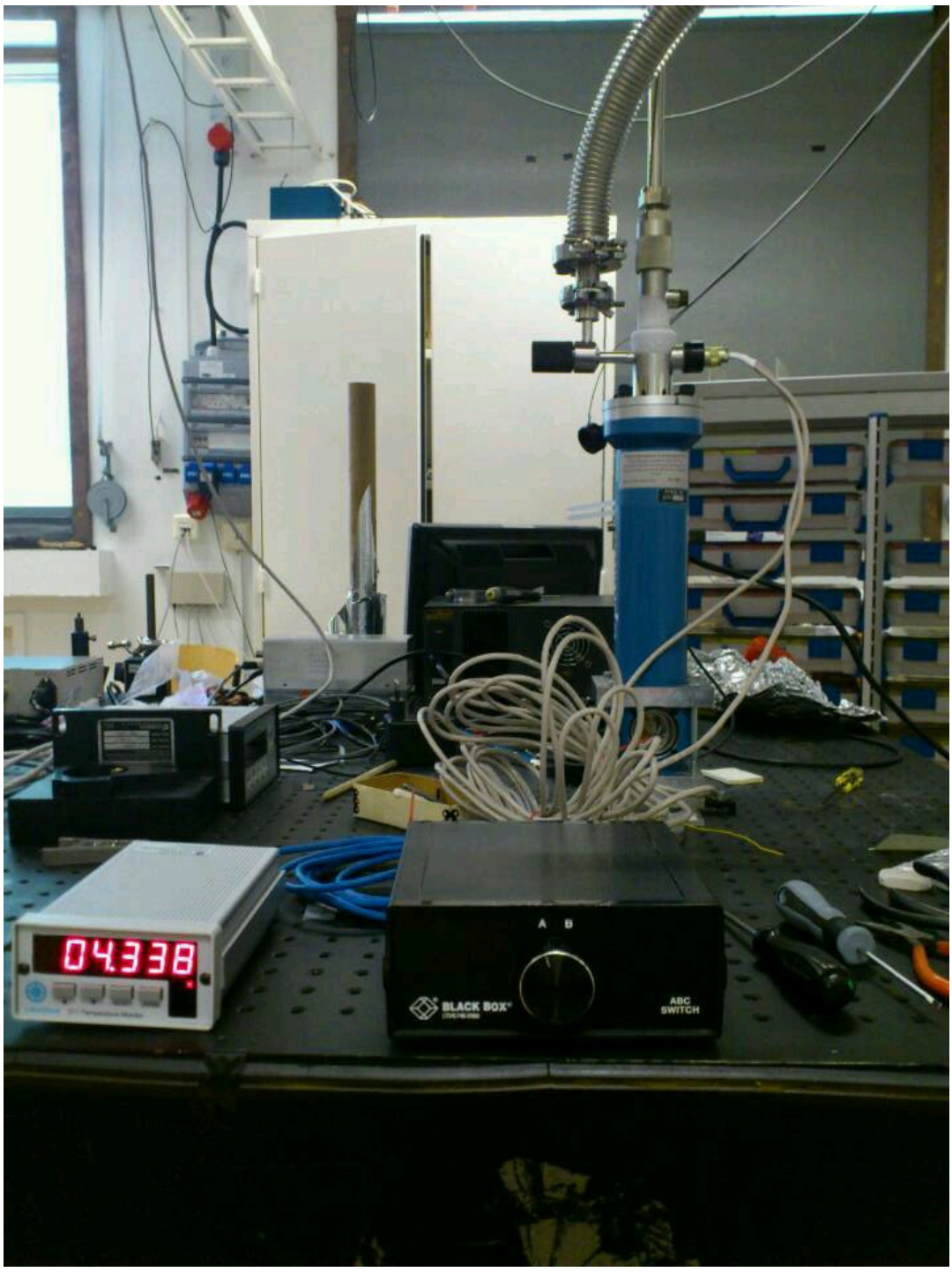

Figure 3.6 (b). The readout of the sensor CU.

The black box in Figure 3.6 (a) is the switch, with readout positions A and B. The readout of sensor A (the sensor CU) is shown in the monitor in Figure 3.6 (b).

3.1.3 Cooling down procedure

Once the sample is fixed on the holder, this one is attached to the cold finger and the temperature sensors are properly installed, the chamber sample is set into a reasonable vacuum (10^{-6} mbar). A vacuum pump it is used for this aim. Then, the liquid Helium

(LHe) is transferred into the cold finger through a transfer tube by a difference of pressure created between the He dewar and the cryostat.

3.1.4 Final setup

In Figure 3.7 the final setup is described. It includes the thermal sensors connection within the cryostat and the temperature readout system composed of the switch box and temperature monitor. All the details can be found in upper section.

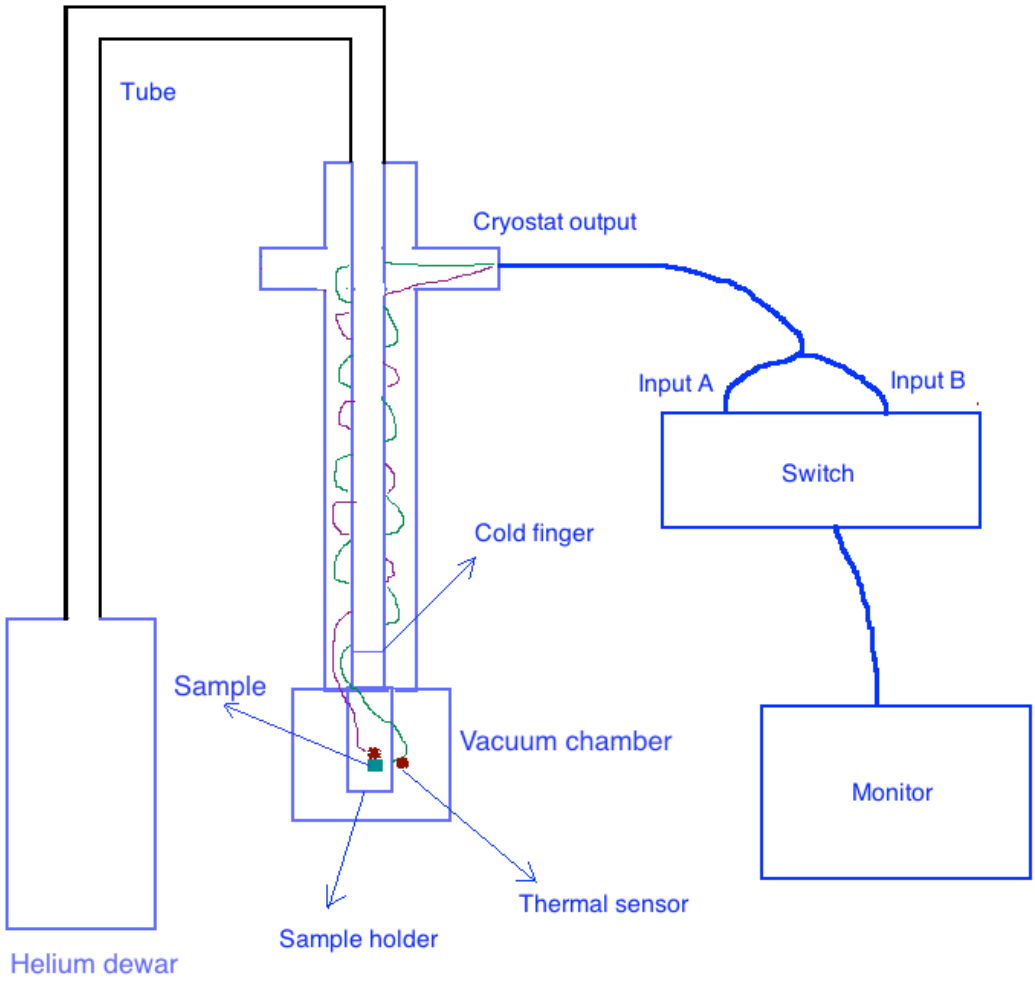

Figure 3.7. Temperature monitor, cryostat and the switch.

3.2 Fluorescence setup

3.2.1 Excitation sources

Two laser sources were used in this thesis. The first one is a dye laser tuned at wavelength of 580 nm. Another one is a diode laser at 370 nm.

3.2.2 Optical setup

The fluorescence setup used for the measurements is shown in Figure 3.8. The green lines are mirror (M1, M2…M6), and the blue lines with arrow represent lenses. Lens 2 is used to collect luminescence from the sample. Other lenses (L1 and L3) are used to focus the excitation beam on the sample. The light blue line on the picture represents an optical filter, which is used to block the laser onto the spectrometer. Several filters can be needed when the excitation power is too high. The position of the sample and the spectrometer are shown in the Figure 3.8. The black line describes laser paths. The dye laser and the UV laser light come from different places, but finally both of them are focused on the sample at the same point. By adjusting the grating position within the spectrometer, emission arising from different spectral regions can be recorded.

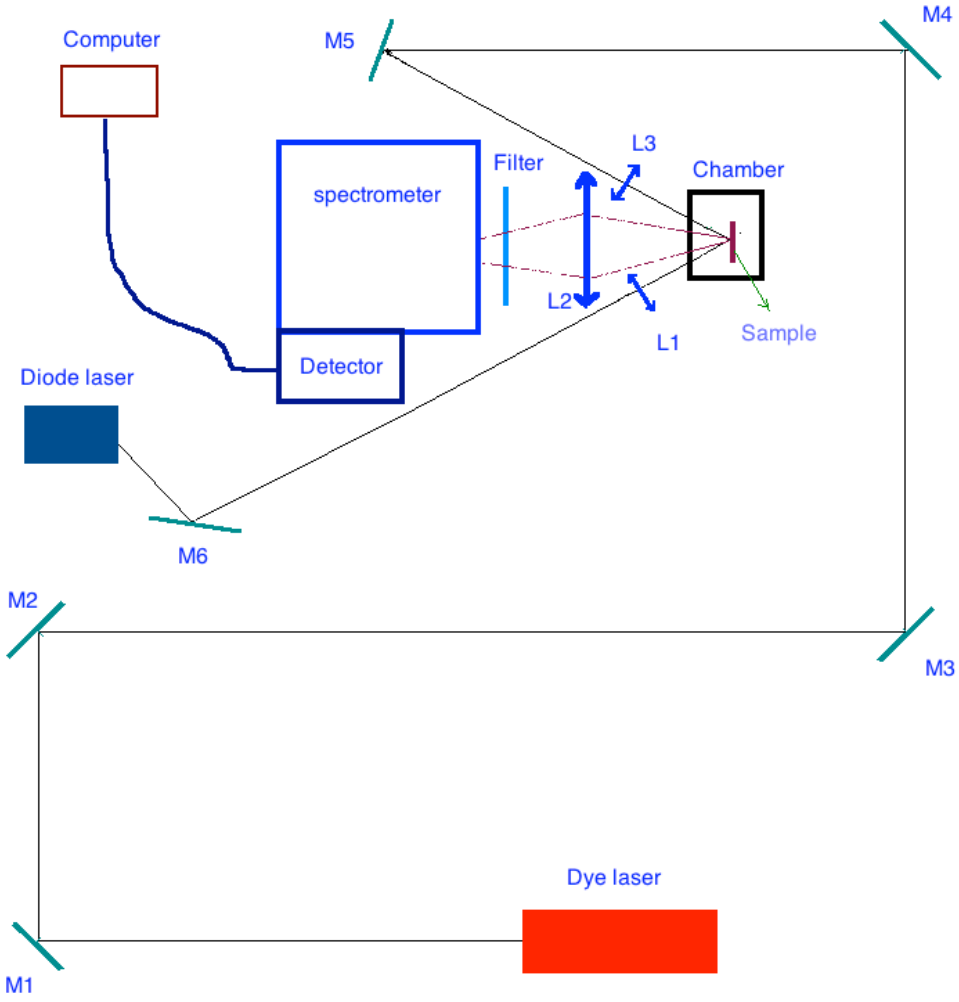

Figure 3.8. Fluorescence setup.

4. Results and discussion

4.1 Temperature tests

In this thesis, the experiments are done under different temperatures. So, the final temperature reached by the sample under investigation as well as the cooling down rate are important to be known. The evolution of the cooling down process for the crystal holder, cold finger and sample are displayed in Table 4.1. The samples used in this thesis are a Ce^{3+}-Eu^{3+} codoped Y_2SiO_5 pellet and an Eu^{3+} codoped Y_2SiO_5 crystal.

Table 4.1. The cooling down process of the holder, the pellet and the crystal sample.

Test sample	*Times (h)*	*Temperature of the cryostat (K)*	*Temperature of the sensor CU*	*Temperature of the sensor SD*	*Flow (L/hour)*
Only holder	0	3.652	9.66	5.265	420
	0.25	3.657	8.104	4.813	420
	0.5	3.684	6.831	4.541	400
	0.75	3.683	6.09	4.389	400
	1	3.682	5.38	4.195	400
	1.25	3.687	5.272	4.132	400
	1.5	3.686	5.126	4.074	400
	1.75	3.681	5.048	4.027	400
	2	3.682	4.981	3.99	400
	3.25	3.675	4.669	3.889	400
With pellet	1	3	3.81	9.19	
	1.5	3	3.51	8.43	
	2.5	3	3.45	7.48	
	3.5	3	3.42	6.86	
	4	3	3.4	6.71	
With crystal	1	4	4.3	6.5	
	2	4	4.1	5.4	
	3	4	4.1	5.2	

All the data above have been plotted by profiles, in order to have an easier way to see the cooling down process. In Figure 4.1 (a), the red line, blue line and the green line represent the temperature of the SD sensor on the holder, the CU sensor on the holder and cold finger respectively. From the data shown in this figure, one can see that the temperature of the sample can reach values around 4.7 Kelvin.

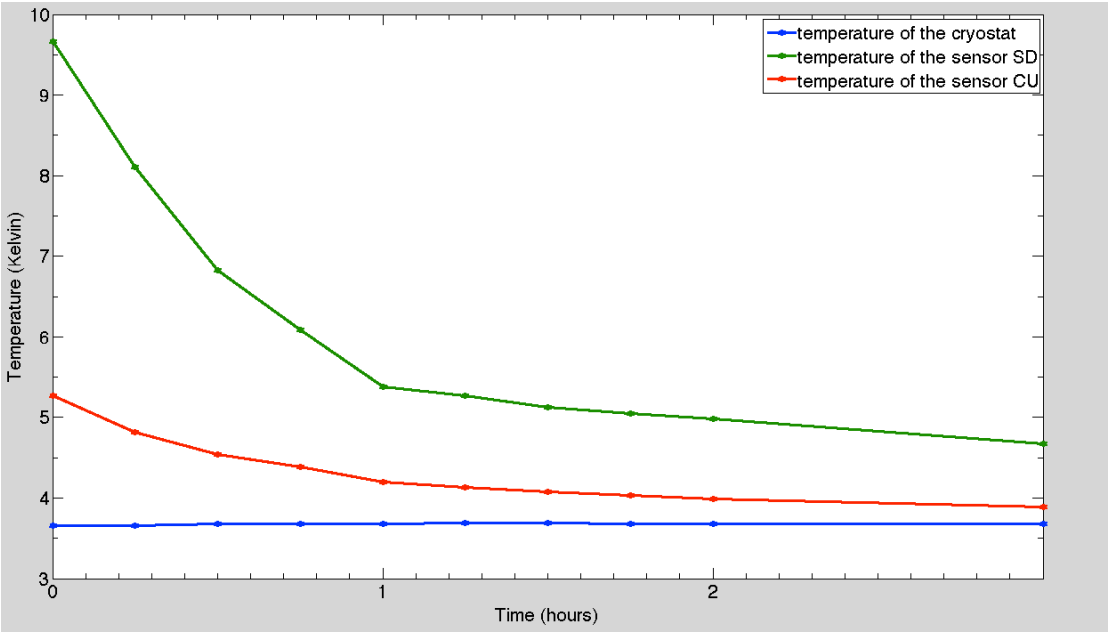

Figure 4.1 (a). Cooling down of the crystal holder and cold finger.

In Figure 4.1 (b), the green line describes the temperature change of the SD sensor on the Ce^{3+}-Eu^{3+} pellet. The red line is the cooling down process of the temperature holder measured by CU sensor. The blue line is the reference temperature of the cryostat.

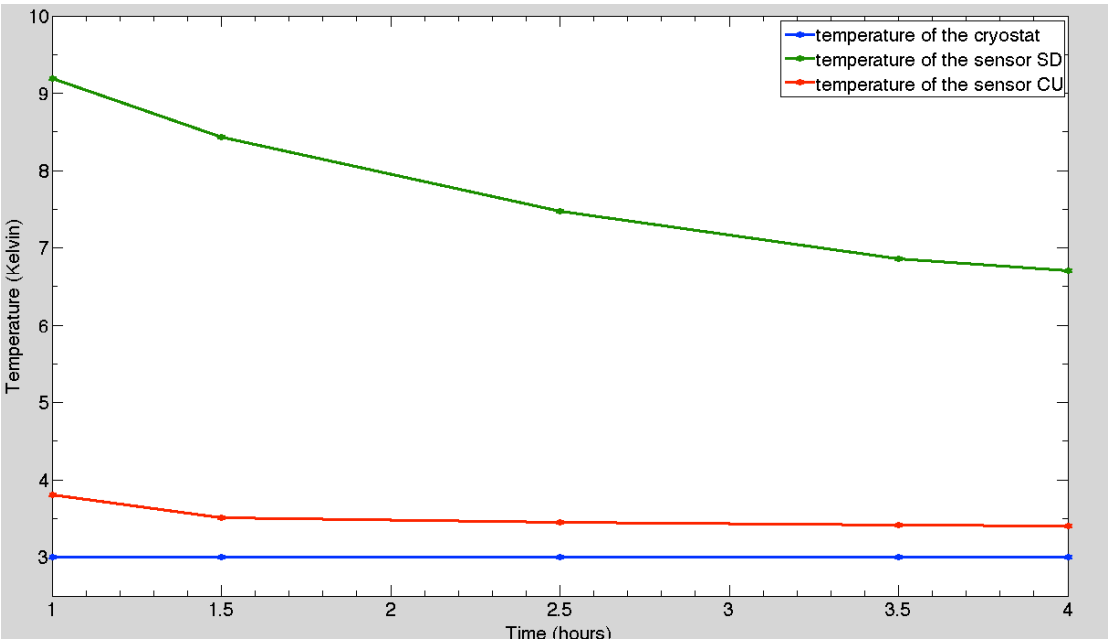

Figure 4.1 (b). Cooling down of the crystal holder, cold finger and Ce^{3+}-Eu^{3+} pellet.

In the figure 4.1 (c), the red line shows the temperature of the sensor SD on the Eu^{3+} crystal. The green line is the temperature of the sensor CU on the holder. The blue line is the temperature of the cryostat.

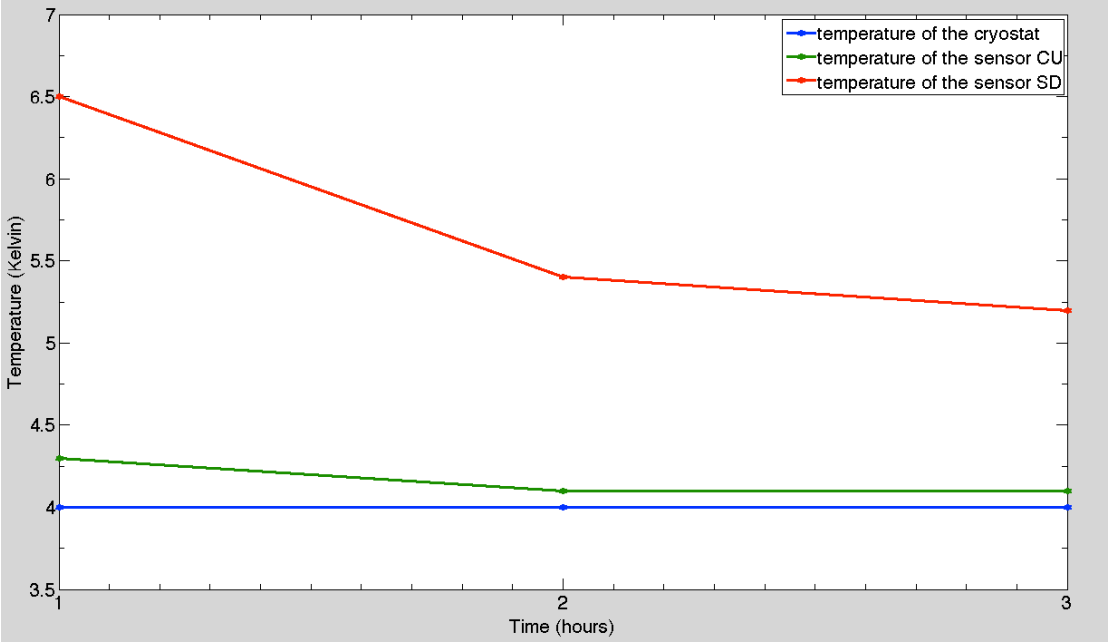

Figure 4.1 (c). Cooling down of the crystal holder, cold finger and Eu^{3+} crystal.

4.2 Fluorescence spectra

4.2.1 Room temperature fluorescence of the Ce^{3+}-Eu^{3+}: Y_2SiO_5 sample.

In Figure 4.2 (a), the red line and the green line are emission spectrum of the sample excited by Dye and UV laser, respectively. The first peak at 576.5 nm is the energy transition from $^5D_2$ to $^7F_5$ as reported by N.C. Chang [10]. The red line at 580 nm is the Dye laser profile. However, the green peak at 580 nm, which is marked by the black spot, is the energy transition from the $^5D_0$ excited state to the $^7F_0$ ground level. The next three peaks marked by blue spots belong to the $^5D_0 \rightarrow {}^7F_1$ transition. The $^5F_1$ level splits into three sub-levels. The $^5D_0 \rightarrow {}^7F_2$ transition appears from 612.2 nm to 627.3 nm. It is marked by blue spots. Five sub-levels due to $^7F_2$ energy level can be seen. There are two peaks marked by red spots around 660 nm. They are assigned to the $^5D_0 \rightarrow {}^7F_3$ energy transition. Finally, the last two peak marked by blue spot around 694.6 and 700.6 belong to the $^5D_0 \rightarrow {}^7F_4$ energy transition.

Under 370 nm excitation, in the case of the Ce^{3+}-Eu^{3+} pellet this is the Ce^{3+} ions which are excited at this wavelength. The Ce^{3+} ions transfer the energy to the Eu^{3+} ions, which subsequently emit photons by the mechanism described in section 2.3.2. Figure 4.2 (b) shows the absorption band of the Ce^{3+} ions and the resonant levels of Eu^{3+}. The energy transfer takes place between the 5d→4f Ce^{3+} transition, and the $^7F_0 \rightarrow {}^5D_4$ Eu^{3+} transition. The excitation decays then by non-radiative processes to the $^5D_0$ level.

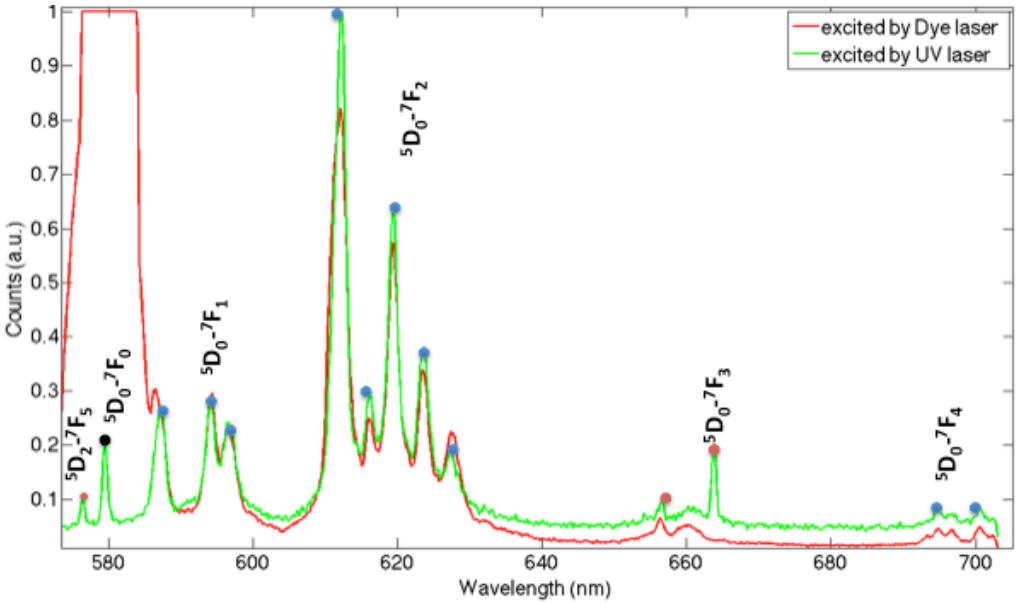

Figure 4.2 (a). Room temperature spectra of the Ce^{3+}-Eu^{3+}: Y_2SiO_5 sample prepared as a pellet, under two excitation wavelengths: 580 nm (red) and 370 nm (green).

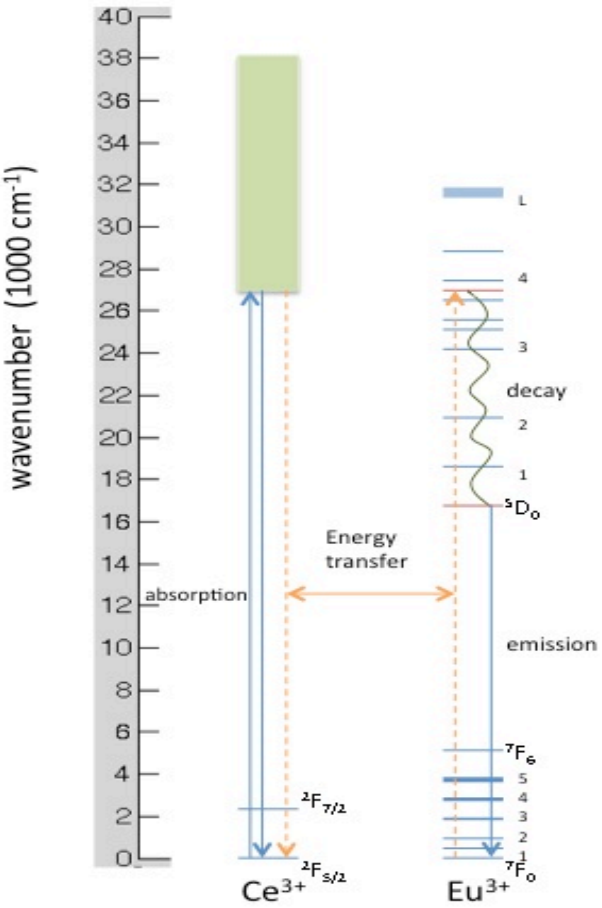

Figure 4.2 (b). Ce^{3+}-Eu^{3+} energy level scheme. Straight arrows represent absorption and emission transitions. Dashed arrows indicate the energy transfer path Ce^{3+}→Eu^{3+} under Ce^{3+} excitation.

4.2.2 Room temperature emission of the Eu^{3+}: Y_2SiO_5 crystal

In Figure 4.3, the energy transitions observed are the same than in Figure 4.2. Although the pellet and crystal samples result from different growing processes (the Eu^{3+} crystal is made under Czochralski growing, providing high quality single crystals), the energy transitions are still not shifted and the emission spectrum remains almost the same. This proves that the growing method used for the Ce^{3+}-Eu^{3+} pellet sample also provides a good quality crystalline sample with similar spectroscopic features as those observed for the Eu^{3+} crystal.

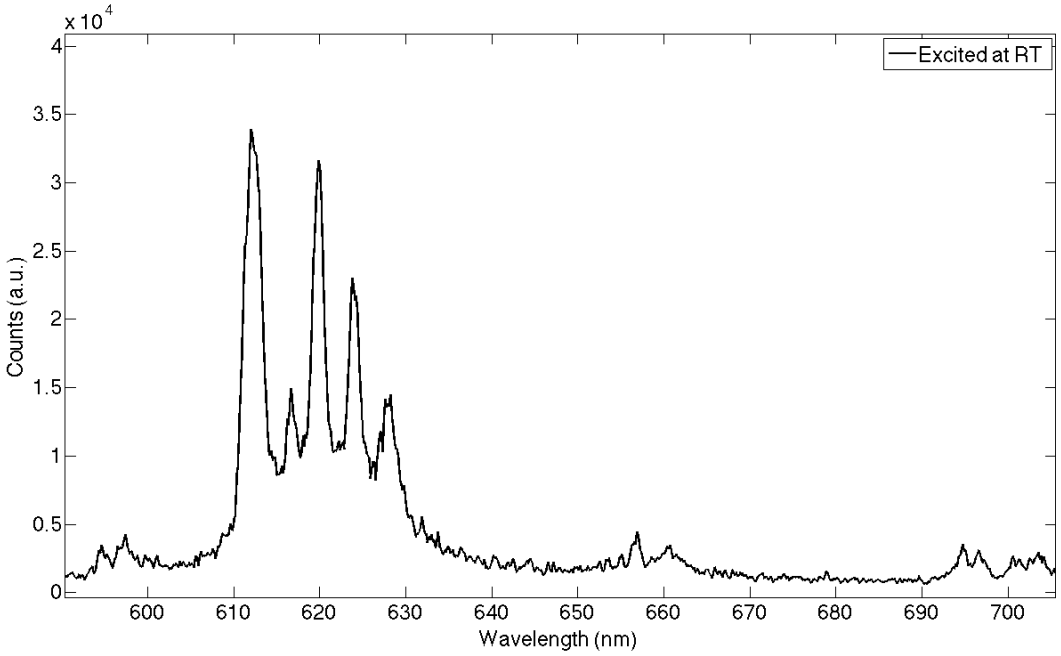

Figure 4.3. Room temperature emission spectrum of the Eu^{3+}: Y_2SiO_5 single crystal under 580 nm excitation.

4.2.3 Eu^{3+}: Y_2SiO_5 emission spectra at 22 Kelvin

Figure 4.4 displays the emission spectrum of the Eu^{3+}: Y_2SiO_5 crystal excited by UV (370 nm) and Dye laser (580) at 22K. Although there is no Ce^{3+} ions acting as a donors, the Eu^{3+} ions is still excited by the 370 nm laser. This result was a bit surprising as no energy level exists for the Eu^{3+} ions at this wavelength. However, this unexpected direct excitation can be explained by the presence of a charge transfer band for the Eu^{3+} ions. The energy is actually absorbed by the charge transfer states and then decays to lower energy levels of the Eu^{3+} configurations.

As shown, the emission spectrum of Eu^{3+} is a bit different for the two cases. At 586.7 nm and 587.8 nm, there are two extra peaks. On the contrary, for the Ce^{3+}-Eu^{3+} pellet, there is only a 587.1 nm emission line. The energy transition $^5D_1 \rightarrow {}^7F_3$ is found at 586.7 nm. On the other hand, at 627.3 nm we find the $^5D_1 \rightarrow {}^7F_4$ energy transition [10].

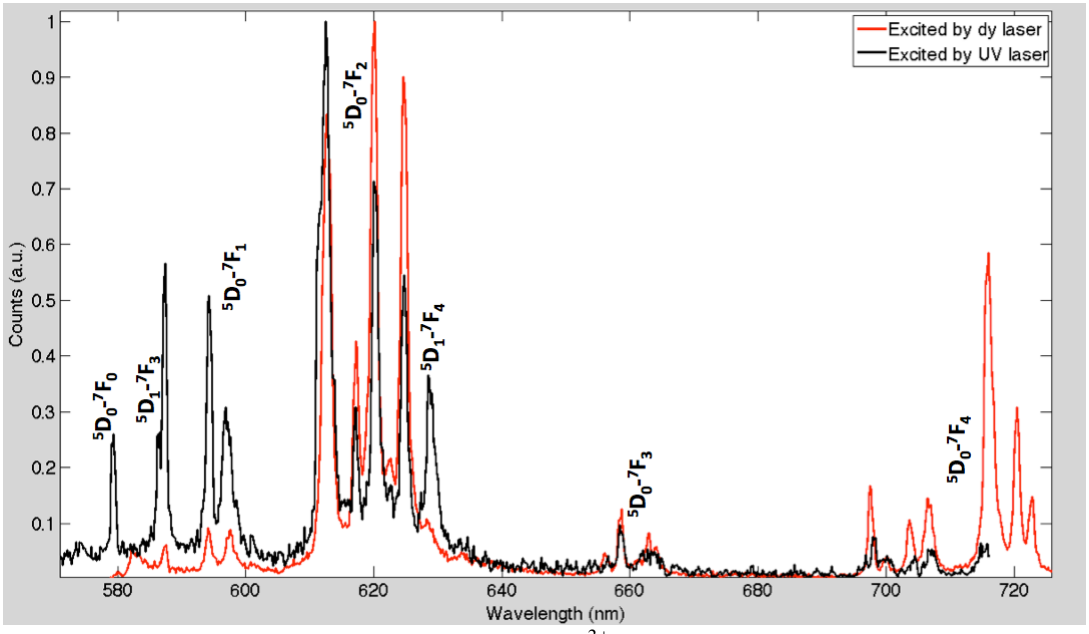

Figure 4.4. Fluorescence spectrum of the Eu^{3+}: Y_2SiO_5 crystal excited by dye (580 nm) and UV laser (370 nm) at 22 Kelvin.

4.2.4 Eu^{3+}: Y_2SiO_5 emission spectra at 4 Kelvin

In Figure 4.5, the energy transitions do not change a lot comparing with the spectra obtained at 22 K. However, at low temperature, the homogeneous broadening becomes weak and lines become sharper. There are some small peaks, which can be seen from 640 nm and 680 nm. They are all from the $^5D_0$ to $^7F_3$ transition as it can be observed in the RT spectrum. The spectrum at 4 Kelvin shows more peak signal from 693 nm to 717 nm all belonging to the $^5D_0 \rightarrow {}^7F_4$ energy transition [10].

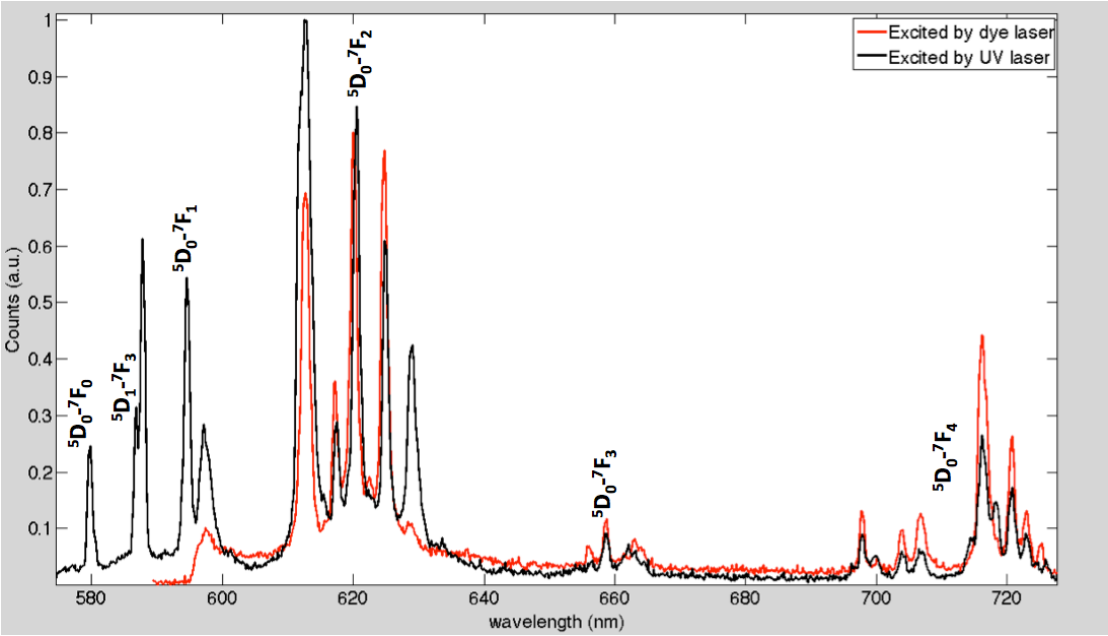

Figure 4.5 Fluorescence spectrum of Eu^{3+}: Y_2SiO_5 recorded under 580 nm and 370 nm excitation at 4 Kelvin.

4.2.5 Comparisons

In Figure 4.7, the emission spectra of Eu^{3+}: Y_2SiO_5 excited by Dye laser at different temperatures is shown. The energy transitions of the Eu^{3+} are almost the same at different temperatures. Only the line broadening is different.

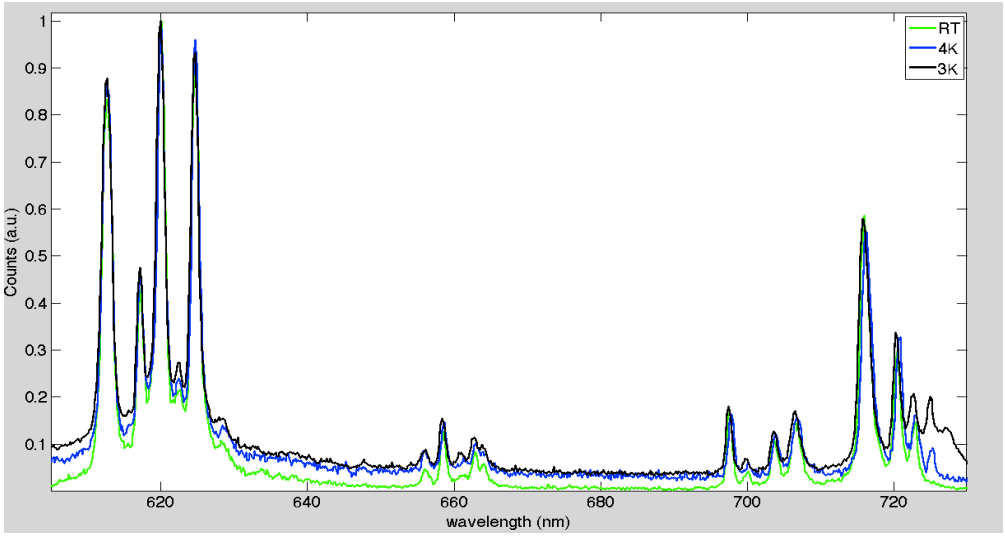

Figure 4.7. Comparison of the fluorescence spectra of Eu^{3+}: Y_2SiO_5 crystal excited by Dye laser at RT, 22 Kelvin, 4 Kelvin and 3 Kelvin.

In Figure 4.8, it is shown the emission spectra of the Eu^{3+}: Y_2SiO_5 crystal excited by UV laser at different temperatures. From the data, we can find that the temperature does not affect the energy level transition, which is the same as Figure 4.7 shows. Comparing Dye laser, the UV laser can make the Eu^{3+} ions to reach higher energy level. So, additional energy transitions appear in this case. For instance, the transition $^5D_1 \rightarrow {}^7F_3$, which is shown in Figure 4.5.

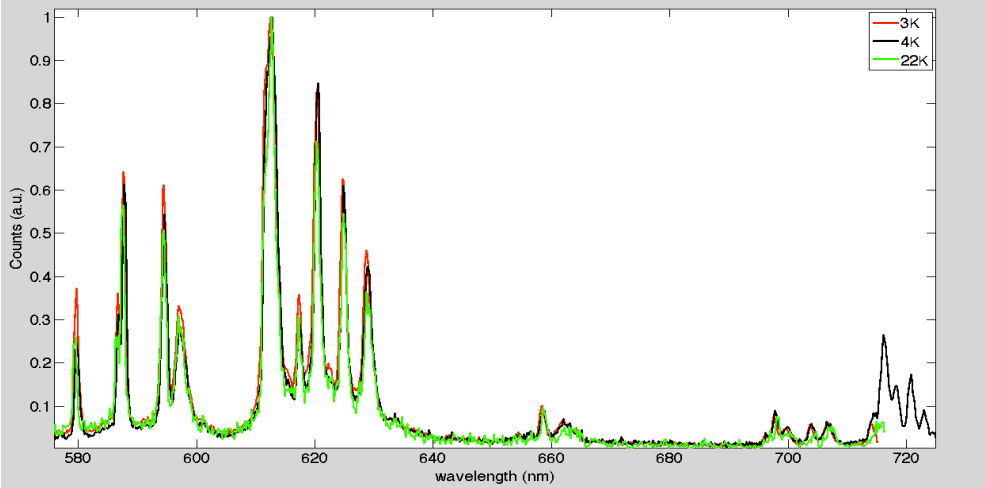

Figure 4.8. Comparison of the fluorescence spectra of the Eu^{3+}: Y_2SiO_5 crystal excited by UV laser at 22 Kelvin, 4 Kelvin and 3 Kelvin.

In conclusion, the analysis of the different emission spectra allows the identification

of the energy transitions of Eu^{3+} within Y_2SiO_5. It is shown that the homogeneous line broadening depends on the temperature, (Figure 4.7 and Figure 4.8). A scheme of the emission transitions of the Eu^{3+} ions has been drawn in Figure 4.9.

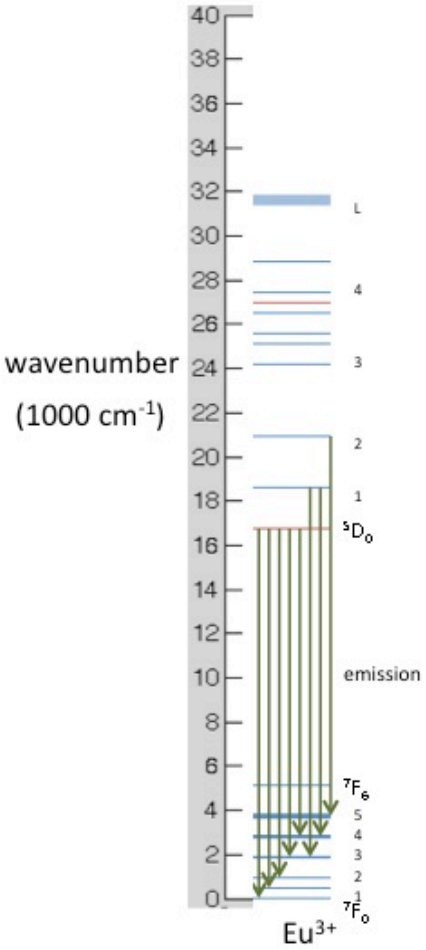

Figure 4.9. The energy transition of Eu^{3+} doped in YSO crystal.

5. Discussion and conclusions

5.1 Suggestion about the improvement of the cooling system efficiency

As shown by the work is done, the temperature of the sample can be cooled down to 4 Kelvin. It means that a good thermal transfer is established between the cold finger, the sample holder and the sample. However, I still have an idea to improve the system cooling efficiency.

The sample is cooled down by contact with the sample holder directly. In order to increase the heat transfer efficiency, it is important to increase the contact area of the sample and the holder. A new holder can be designed to solve this problem. It can cover more faces of the sample instead of covering one face of the sample. I think the system cooling efficiency should be improved in this way.

5.2 Suggestion about the improvement of fluorescence detection

Actually, the resolution of the spectrometer in this thesis is good. We can see a lot of emission lines, which are expected to be seen. For instance the $^5D_0 \rightarrow {}^7F_0$ emission line (580 nm), when the Eu^{3+}: Y_2SiO_5 crystal is excited by the UV laser (370 nm). However, if the resolution of the spectrometer used in this thesis could be better, more emission lines will be seen from the spectra of Eu^{3+} ions. As a result, how the crystal field can influence the energy transition of Eu^{3+} ions could be studied.

5.3 Summary of the work

In this thesis, an optical fluorescence setup has been designed. The measurements were performed at cryogenic temperature. The cooling down process and the temperature reached by the sample was controlled by two temperature sensors installed within the cryostat. The spectra of the Ce^{3+}-Eu^{3+} pellet and Eu^{3+} crystal have been measured. By analyzing the data, the Eu^{3+} emission transitions could be assigned. And also, Ce^{3+}-Eu^{3+} pellet sample, grown by a different growing method than the Eu^{3+} single crystal has been proved to be of good quality. This is supported by the fact the emission spectrum of the Eu^{3+} ions in the Ce^{3+}-Eu^{3+} pellet is the same as that in the Eu^{3+} crystal. The Eu^{3+} crystal is grown by the Czochralski method, which is known to provide high quality crystalline samples. By doing this thesis, we have a good initial vision of the Ce^{3+}-Eu^{3+} codoped Y_2SiO_5 spectroscopic features.

6. Acknowledgement

Firstly, I want to show my sincerely gratitude to Stefan Kröll for allowing me to do my diploma study here. And I would like to say thank you so much to my supervisor Diana. Thanks for you bringing me into the science, your patience and your smile. I have learned a lot of knowledge of solid physics and spectroscopy by your help.

Secondly, I must say, I love to study and work in this group because of you: Qian, Jenny, Lars, and Andreas. All the suggestions I got from you help me solve the problem efficiently. The weekly group meeting and fika time with you all have been good memories to me.

Finally, I want to show my best wishes to my parents and Q. Wu, thanks for the supports during my study in Sweden.

7. Reference

[1] L. Rippe. "*Quantum computing with naturally trapped sub-nanometre-spaced ions*", PhD thesis, Lund University (2006).

[2] S. B. Poole, D. N. Payne, R. J. Mears, M. E. Fermann, and R. I. Laming. "*Fabrication and Characterization of Low-Loss Optical Fibers Containing Rare-earth ions*", Lightwave Technology Vol: 4, 7, 870-876, (1986).

[3] U. Paul, "*Review of rare earth doped fiber lasers and amplifiers*", Optoelectronics 135, 385-407, (1988).

[4] T. Bladh. "*Single ion detection setup*", Master thesis, Lund University (2013).

[5] G. Liu, B. Jacquier. *Spectroscopic properties of rare earths in optical materials*, Springer (2005).

[6] C. J. Foot, *Atomic Physics*, Oxford, (2005).

[7] S. Svanberg, *Atomic and Molecular Spectroscopy*, Springer, (2003).

[8] G. H. Dieke and H. M. Crosswhite, "*The spectra of the doubly and triply ionized rare earths*", Applied Optics, 2 (7), 675, (1963).

[9] G. S. Ofelt. "*Intensities of crystal spectra of rare-earth ions*", Chemical Physics 37, 511, (1962).

[10] N.C. Chang and J.B. Gruber, "*Spectra and energy level of* Eu^{3+} *in* Y_2O_3", Chemical Physics 41, 3227, (1964).

[11] Y. Yan, "*Towards single Ce ion detection in a fulk crystal for the development of a single-ion qubit readout scheme*", PhD thesis, Lund University, (2013).

[12] T. Förster, "*Zwischenmolekulare Energiewanderung und Fluoreszenz*" Annalen der physik 437, (1948)

[13] D. L. Dexter. "*A Theory of sensitized Luminescence in Solids*", Chemical Physics. 21, (1953)

[14] F.R. Fickett, "*Oxygen annealing of copper: A review*", Materials science and engineering, 14, 199-210, (1973).

[15] A. R. Kerr and N. Horner, "*The low temperature thermal resistance of high purity copper and bolted copper joints*", Electronics division technical note, 163, (1991).

[16] Instructions, Silicon diode and GaAlAs diode temperature sensor installation, Model DT-470,471,670, and 671 CU and DI packages, and TG-120-CU package, Lake Shore.

[17] www.physics.gla.ac.uk/~kskeldon/PubSci/exhibits/E3/